Brazilian Journal of Geophysics, 43 (2025) 1, 1-20
Brazilian Geophysical Society
ISSN 2764-8044
DOI: 10.22564/brjg.v43i1.2335

INTEGRATION OF AIRBORNE AND GROUND GEOPHYSICAL PROSPECTING APPLIED TO AN EPITHERMAL GOLD DEPOSIT IN THE CASTRO BASIN, SOUTHERN BRAZIL

Francesco Antonelli[1]*, Rodoilton Stevanato[1], Angela Rodizes[1], Vinicius Serrano[2], Jorge Kazuo Yamamoto[2], Gustavo Abreu[2], Francisco José Fonseca Ferreira[1], and Maximilian Fries[1]

[1]Universidade Federal do Paraná - UFPR, Curitiba, PR, Brazil
[2]Universidade de São Paulo - USP, São Paulo, SP, Brazil

*Corresponding email author: francescoantonelli.geof@gmail.com

ABSTRACT.
The gold exploration in the Castro Basin, Brazil, has been hampered by complex geology, disseminated low-grade ore, and the subsurface nature of quartz-adularia veins. To address these challenges, this study applied airborne geophysical techniques (gamma-ray spectrometry and magnetometry) to identify hydrothermal alteration zones and related structures. Radiometric parameters and magnetic gradient variations were analyzed to correlate with gold occurrences. Results indicated a strong association between potassium enrichment and magnetic lineaments, which was confirmed by geochemical samples. Based on these results, the Torre Target was selected for ground geophysical surveys. Electrical resistivity, induced polarization and magnetometry data were collected and integrated with digital elevation models. Geoelectrical sections and maps delineated the main ore body characterized by high chargeability anomalies associated with argillic alteration and disseminated sulfides. Resistivity data highlighted potential vertical contacts and fault structures indicative of an epithermal system. Magnetic techniques identified areas of magnetite concentrations within breccias and rhyolite, suggesting a connection to the mineralization events. In addition, magnetic data helped differentiate chargeability anomalies associated with the ore body from those associated with residual soil from diabase dikes. Results were validated by drilling, confirming the accuracy of the targets identified. This study demonstrates the effectiveness of geophysical techniques for the exploration of challenging gold deposits in the Castro Basin.

Keywords: magnetic and radiometric data integration; geoelectrical methods; airborne geophysics; advancing gold exploration.

INTRODUCTION

Geophysical prospecting methods have been an invaluable tool in mineral exploration for over a century (Hoover et al., 1992). Its success lies in its ability to provide information and insights into subsurface geology. By combining geophysical data with geological information,

topographic data, mineralogical and geochemical analysis, exploration teams can effectively define target areas. However, it is critical to select the appropriate geophysical methods for each prospect, as deposit characteristics can vary significantly (Irvine and Smith, 1989).

Epithermal low-sulfidation deposits often yield suboptimal geophysical responses due to the formation of alteration zones by hydrothermal processes associated with rock intrusions, which can complicate the differentiation of geological units. Furthermore, the physical properties of the rocks typically exhibit low contrast, which presents a challenge in distinguishing the alteration halo. Despite these difficulties, indirect methods are still regarded as the most effective for prospecting gold mineralization in these environments, as evidenced by various studies (Feebray et al., 1998; Irvine and Smith, 1989; Allis, 1990; Morrell et al., 2011).

The formation of iron oxides, silicification, and an increase in clay content within the rock matrix are typical hydrothermal events (White and Hedenquist, 1995; Hedenquist et al., 2000). These processes result in notable alterations to the physical properties of epithermal rocks, including elevated concentrations of potassium and potentially uranium, modifications in the magnetic properties of minerals, and the emergence of high chargeability zones, frequently associated with near-vertical conductive structures (Irvine and Smith, 1989; Allis, 1990; Airo, 2001; Airo and Mertanen, 2008). Additionally, density variations may occur due to crystallization and accretion of new minerals, such as metal sulfides disseminated infilling rock pores and cavities (Irvine and Smith, 1989).

The objective of this research was to integrate airborne and ground geophysical data to identify promising areas for gold prospecting in the Castro Basin. This entailed first understanding the magnetic-structural framework and mapping radiometric signatures related to hydrothermal activity at a regional scale using airborne data. Thereafter, the investigation focused on specific targets to apply detailed ground methods and identify the main ore deposits.

GEOLOGICAL SETTING

The Castro Basin, located in the southern region of Brazil in the state of Paraná, represents a Neoproterozoic rift (1 Ga - 541 Ma) that is characterized by extensional tectonics (Almeida et al., 2010). The basin is primarily composed of rhyolite, andesite, and volcaniclastic rocks of acidic to intermediate composition, spanning from the Early Cambrian (543 Ma) to the Early Ordovician (490 Ma) (Reis Neto et al., 1994). In accordance with the findings of Silva and Vaine (2001), the Castro Group is subdivided into five principal units; (I) The Lower Sedimentary Association comprises Arcosian sandstones and siltstones; the (II) Upper Sedimentary Association is represented by alluvial fans with polymorphic conglomerates; The (III) Volcanic Acid I category includes quartz-rich breccias, tuffs, and ignimbrites; (IV) Volcanic Acid II, which is distinguished by the presence of rhyolites; and (V) Volcanic Acid-Intermediate, which is characterized by andesites, volcanic tuffs, ignimbrites, and subordinate conglomerates (Figure 1).

Lithological units and structural features present NW-SE direction, given by the diabase dyke swarm from Cretaceous (127 - 160 Ma), or NNE-SSW direction through the central shear zone developed during extensional drifts of the South American Platform breaking. Castro Fault separates the sedimentary basin from the Ediacaran granitoids from Cunhaporanga Complex at east, while around the basin is bordered by Silurian and Devonian (416 - 359 Ma) sedimentary rocks from the Furnas Formation of the Paraná Basin (Mapa et al., 2016; Mapa et al., 2019).

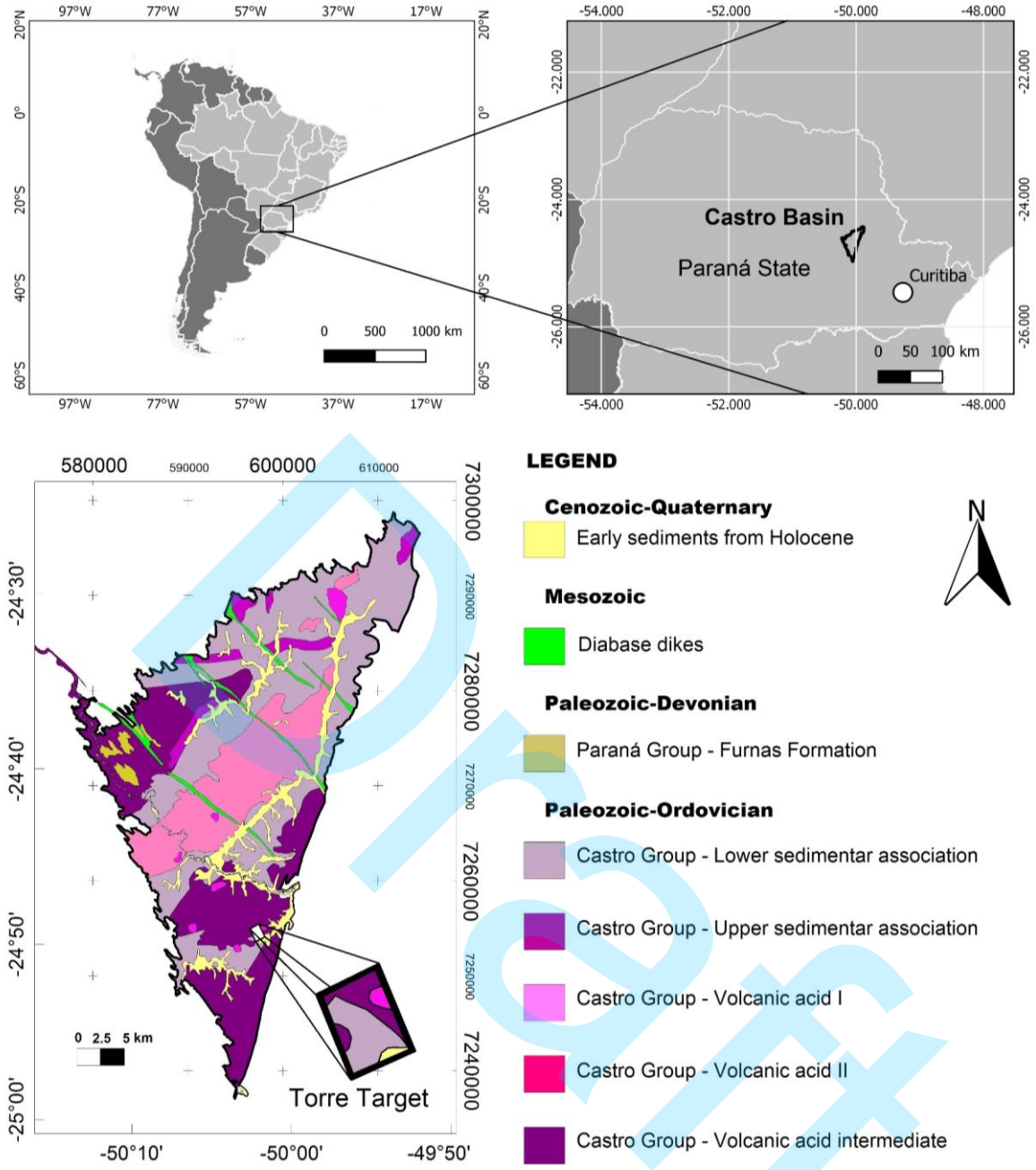

Figure 1 – Location and geologic map of Castro Basin and Torre Target.

Major deposits of gold (Au) in the Castro Basin occur associated with shallow intrusions at low angle normal faults in a low-sulfidation (LS) epithermal system. A positive correlation was observed between the silica increase and Au occurrence where most of the important mineralization zones are seen disseminated in veins composed of quartz, adularia, sericite and chalcedony. Vein intrusions normally lie between rhyolite domes and hydrothermal altered siltstone rocks. Outside silica enrichment mineralization is seen with great association with clays minerals of illite group. Breccias and volcanic acid rocks also have a good association with Au but with less content (Seoane, 1999; Mapa et al., 2016; Mapa et al., 2019).

Following the preliminary results, a small target area known as the Torre Target was selected for detailed investigation. The area encompasses a rectangular polygon of 0.851 km², situated within UTM zone 22J (WGS 84 datum), and is defined by the following coordinates: 597,559E / 7,255,571N; 598,169E / 7,254,127N; 597,130E / 7,253,673N; and 596,575E / 7,255,069N.

MATERIAL AND METHODS

State of art

Gamma- ray spectrometry is a passive geophysical method that is widely employed in geological mapping and in the identification of regions with potential economic mineral deposits (Reynolds, 2011). The variations in the concentrations of potassium (K), thorium (Th), and uranium (U) in rocks are influenced by their mineralogical composition, which is affected by both internal factors, such as the geological history of the unit, and external factors, such as erosional processes that alter the recorded concentrations. For example, an increase in the silica content of igneous rocks is frequently accompanied by elevated concentrations of uranium and thorium. Consequently, felsic rocks typically exhibit higher levels of these radioelements in comparison to mafic or ultrabasic igneous rocks (Scott and Dickson, 1997; Ribeiro et al., 2015). This approach enables interpreters to distinguish between granitic bodies, secondary surface processes, and potential mineralization associated with hydrothermal fluids. Such interpretations are enhanced by generating ratios and factors that highlight anomalous concentrations of these elements (Ribeiro et al., 2015). Although its depth range is limited, this method remains a key geophysical tool in geological mapping, delivering lithological information comparable to that obtained from on-site surveys.

As defined by Dentith and Mudge (2014), magnetometry is the measurement of variations in the Earth's magnetic field attributed to crustal inhomogeneities. Consequently, the magnetometric method is employed to investigate contrasts in magnetization across different media. These variations are attributed to the magnetic properties of rocks, which are in turn related by magnetic susceptibility, defined as a quantitative measure of a material's capability to interact with and distort an applied magnetic field. The magnetic field at any point on Earth's surface is influenced by both magnetic induction and remnant magnetization. The magnetization vector is the vector sum of these two components.

Geoelectric methods are largely employed due to their versatility, being easily adapted for almost all investigative tasks (Reynolds, 2011). It relies on the physics of current flow in the earth. Electrical resistivity (Res) measures the apparent resistivity (ρa) of the subsurface between two points on Earth's surface in the application of a controlled electric current through the subsurface at other two points. Apparent resistivities are differentiated by voltage variations (ΔV), also known as potential differences (ddp), detected by voltmeters.

Considering the geometric factor of each measurement, ΔV and current (I) are used to calculate the "real" resistivity. The unit in the International System of Units (SI) is Ohm.meter (Ω.m), representing the resistance faced by charged particles during flow. The final resistivity model is obtained through matrix inversion. The induced polarization (IP) method measures the small residual voltage as a function of time or frequency. The IP effect occurs when certain soil particles and minerals, acting like capacitors, store charges, causing a delay in the transient current decay. This results in a slower-than-normal disappearance of the electric field after the current is suspended. In the time domain, voltage is measured in milliseconds, and the response is a decreasing exponential curve (V x t). This method is widely used in mining prospecting to locate disseminated sulfides or other metallic deposits and associated ores (Sumner, 1976). It can also be employed as an auxiliary method in hydrogeological studies (Reynolds, 2011).

Data Acquisition

Terrestrial data acquisition included six geoelectric profiles (L1-L6) and seven magnetic profiles (L1-L7) totaling 5.7 km and 7 km of linear coverage, respectively. For all methods, stations or readings

were spaced 25 meters apart in a N60E direction. This direction was chosen to perpendicularly intersect the main structure of the mineralized vein (N60W).

Iris Instrument Vip3000 and Elrec Pro 10 channel systems were used for Induced Polarization (IP) and resistivity data. The dipole-dipole array was used with 8 "n" levels spaced 25 meters apart. IP measurements were made in the time domain and cole-cole diagram using 5 current pulses of 2 seconds each, coinciding with the resistivity measurement intervals. Non-polarizable electrodes and individual flexible copper cables were used in the survey.

Magnetic acquisition was performed using the Scintrex ENVIMAG CS sensor magnetometer. We collected 1 or more reading for each station of measure and saved all in one single database. The tie point method was used to correct diurnal variations in the geomagnetic field.

Elevation and x and y coordinates were measured using the GS18 T GNSS mobile from Leica GeoSystems.

Data processing

The aerogamma-ray spectrometry and aeromagnetic data used in this research were obtained from the Paraná-Santa Catarina Aerogeophysics Project. This project was conducted from November 10, 2009, to August 8, 2011, spanning 689 calendar days and 513 flight hours. It was carried out by Lasa Prospecções S.A. on behalf of the Geological Survey of Brazil (Companhia de Pesquisa de Recursos Minerais do Brasil - CPRM). The airborne geophysical survey covered 140,397.98 km of high-resolution aeromagnetic and aerospectrometric profiles, and an area of 65.562 km² encompassing sections of the states of Paraná and Santa Catarina. Acquisition parameters employed for the project can be found in Table 1.

Table 1 – Specifications per acquisition parameters extracted from CPRM (2011).

Acquisition Parameters	**Specifications**
Nominal height	100 m
Flight lines direction	N-S
Flight lines spacing	500 m
Total number of flight lines	462 (133,682.89 km)
Control lines direction	E-W
Control lines spacing	10,000 m
Total number of control lines	54 (6,715.09 km)
Aeromagnetometer	Scintrex CS-3
Gamma-spectometer model	Exploranium GR-820
Interval between consecutive geophysical measurements	0,1 s (magnetometer) and 1,0 s (spectrometer).
Airplane average speed	PR-FAG: 269 km/h PT-WOT: 276 km/h PR-LDS: 284 km/h

The processing of gamma-ray spectrometry involved the interpolation of the channels for potassium, uranium, and thorium content of the original gamma-spectrometric database, which was conducted using the minimum curvature method. This interpolation employed a regular square grid with dimensions of 125 m x 125 m, which is one-quarter of the spacing between the flight lines.

Individual gamma-ray channels were expressed as percentages for potassium (K) and parts per million (ppm) for uranium (U) and thorium (Th). This data was gridded using minimum curvature interpolation (Briggs, 1974) with a cell size of 125 m for both data sets. This grid size represents one quarter of the spacing between acquisition lines.

The F factor is a calculated value that assesses the relative abundance of radioelements in a sample. It is determined by multiplying the potassium (K) content and uranium equivalent (U_{eq}) by a factor and then dividing by the thorium equivalent (Th_{eq}). This ratio is useful because K and U_{eq} are more prone to redistribution, while Th_{eq} remains relatively stable under most conditions (Gnojek and Prichytal 1985, Scott and Dickson, 1997).

$$F = K\ X\ \frac{eU_{eq}}{Th_{eq}} \tag{1}$$

The magnetometry data was subjected to a sequential process of data correction with the Oasis Montaj 8.3 Geosoft software. Once collected, the magnetic data was corrected for diurnal variation and the IGRF was removed. The International Geomagnetic Reference Field (IGRF) calculated for the date and geographic location was 22,575.7 nT. The Total Magnetic Intensity (TMI) map was generated using the minimum curvature method.

To reduce the bipolarity of the magnetic sources and simplify the interpretation of the anomaly, the TMI grid was reduced to the pole (RTP). Paleomagnetic studies showed that the majority of diabasic rocks of the Ponta Grossa Arch Formation have remnant magnetization in normal polarity (Raposo and Ernesto, 1995), suggesting that the geomagnetic field during the rock formation was like today. By this knowledge we can consider only the induced magnetization and ignore the influence of remanence on the magnetization direction (Weihermann et al., 2018) once this enables the technique of reduction to the pole (RTP) without collateral effects (Baranov and Naudy, 1964; Li, 2008). Based on the site location, the data were reduced to a magnetic pole assuming an inclination (I) = -33.87, declination (D) = -18.38 and correcting the amplitude to -56.13 nT. First tested on synthetic data using a model composed of two prisms (P1 and P2) with different depths and dimensions (Figure 2), the RTP showed symmetry and could be better used preceding the tilt angle derivative (TDR) filter and finally be performed on real data.

The TDR (Miller and Singh, 1994) is an enhancement filter that basically centralizes the maximum of the anomaly with its causative source and equalizes magnetic amplitudes in potential data, limiting values between -1.57 and 1.57 rad. This filter is widely used to trace magnetic lineaments and enhance signals from deep sources and to enhance signals from deep sources.

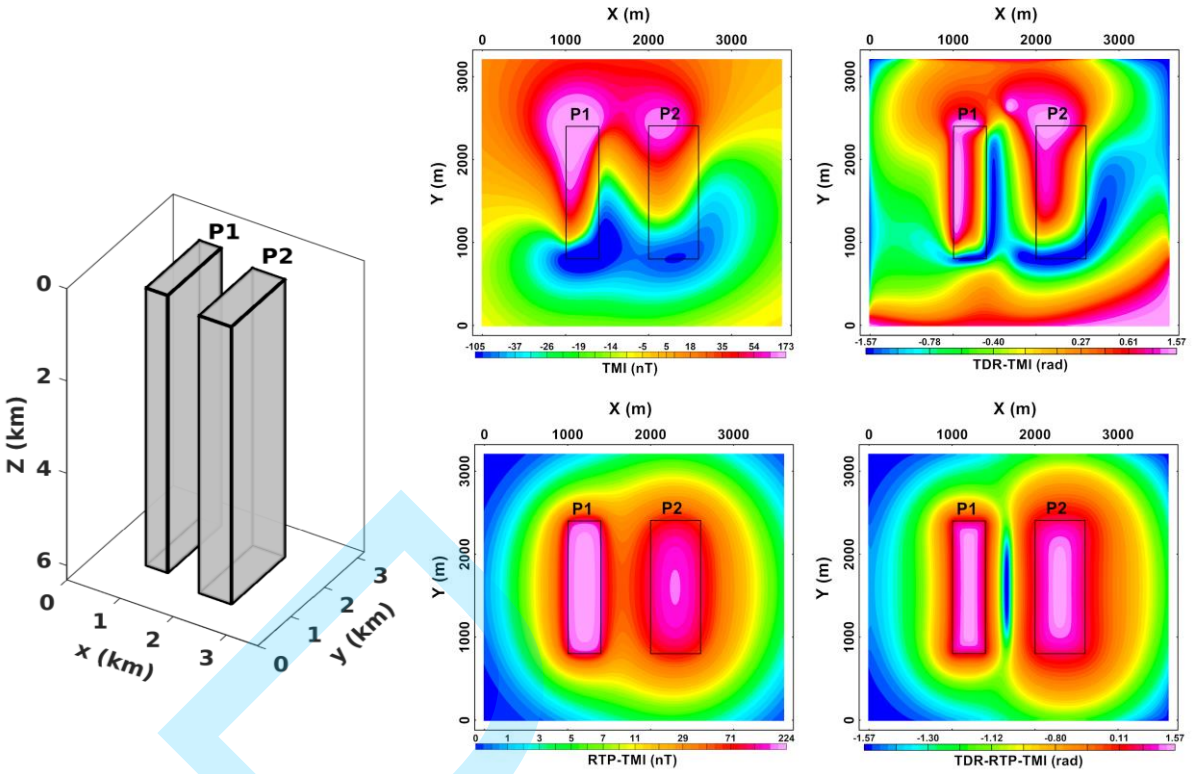

Figure 2 – Synthetic model of prisms (P1 and P2) with dimensions of P1: 1 km (y) x 0.3 km (x) 6 km (z) starting at 100m of depth and P2: 1 km (y), 0.7 km (x) and 6 km (z) starting at 200m of depth and magnetic responses from synthetic data. Comparison between Total Magnetic Intensity (TMI), TDR_TMI, RTP_TMI and TDR_RTP_TMI anomalies.

For airborne data, an upward continuation of 100 meters was applied to the reduced-to-the-pole grid (RTP-TMI), resulting in a total equivalent height of 200 meters (given the aircraft altitude of 100 meters). For ground RTP data, an upward continuation of 50 meters was applied. This low-pass filter was applied to further enhance the clarity of deeper structures and eliminate noise from shallow sources.

Due to the massive influence of the Ponta-Grossa dike swarm in the study area, which completely masks the signals of deep sources, the subsequent operation was divided into two branches. In one branch, a directional cosine filter with a cutoff angle of 145° (DC145°) was applied to the right side to reject the signal from dykes that are predominantly parallel to this direction. On the left side, the DC145° filter was not applied to preserve all structural features, knowing from literature that in the same direction of dykes is also a preferential direction to mineralized veins intrusions (Serrano, 2018). The final step was concluded with the production for both grids and with a manual procedure of magnetic traces. The lineaments were generated at the center of the TDR_upw100m_RTP_TMI and TDR_DC145°_upw100m_RTP_TMI grids with a fixed zoom scale of 1:250,000. The processing of aeromagnetic data followed the workflow outlined in Figure 3.

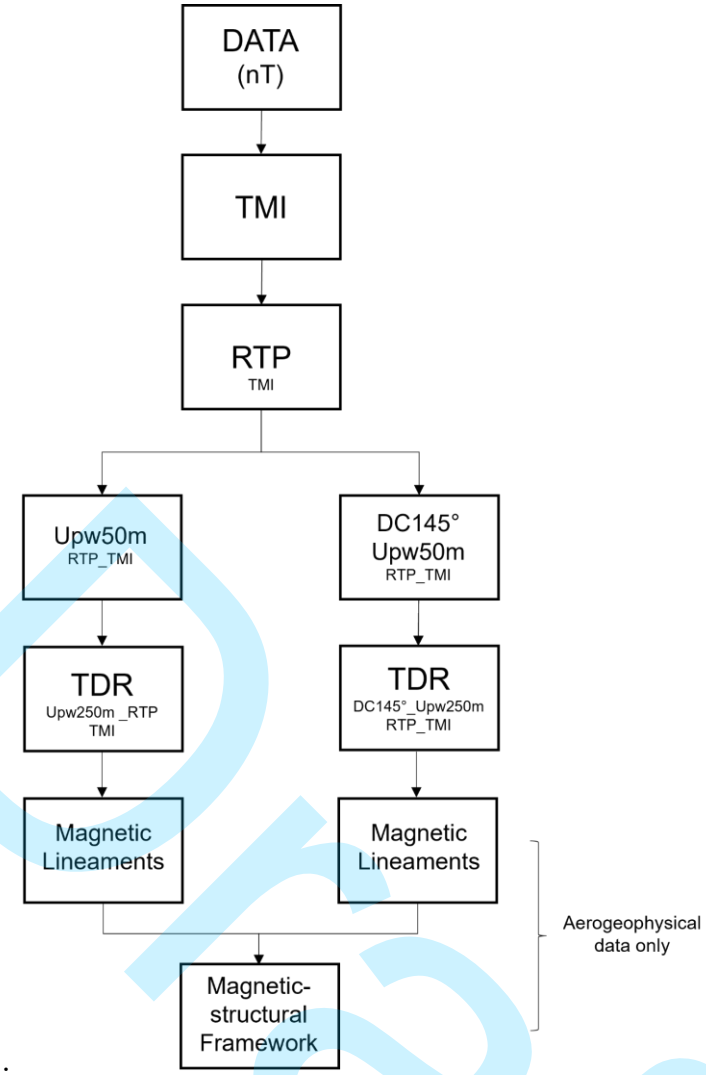

Figure 3 – Aeromagnetic and magnetic data processing flowchart.

The Triangulated Irregular Network (TIN) interpolation method was applied to generate the digital elevation model (DEM) grid, using a cell size of 50 meters. To analyze the DEM-derived lineaments, scales of 1:50,000, 1:250,000, and 1:400,000 were employed for comparison with the frequency distribution of lineaments interpreted from TDR magnetic data.

RESULTS

Elevated potassium concentrations suggest an association with volcanic acid I and II units of the Castro Group. Uranium and thorium concentrations are slightly higher in Arcosian sandstones and siltites of the lower sedimentary association within the Castro Group.

The F factor, with cutoff values above the median (>0.177) and 2x the median, was used to identify hydrothermal alteration. This factor showed a strong correlation with gold (Au) bearing geochemical assays and with the N45W and N45S oriented magnetic structural lineaments (Figure 4). A clear correlation was observed between geophysical features and higher gold contents (≥ 25 ppb) in geochemical samples gold occurrences reported by various authors (Lopes et al., 1969; Arioli and Moreton, 1982; Seoane, 1999; Mapa et al., 2016; Mapa et al., 2019).

Magnetic maps of the Torre Target area (Figure 5) show a prominent northwest trending anomaly that is consistent in amplitude with diabasic rocks. Also, this anomaly is located on a topographic 145° lineament slope and with a magnetic lineament traced on the TDR_upw100m_RTP_TMI and TDR_DC145°_upw100m_RTP_TMI maps present in the regional of Castro's prospectivity of gold map.

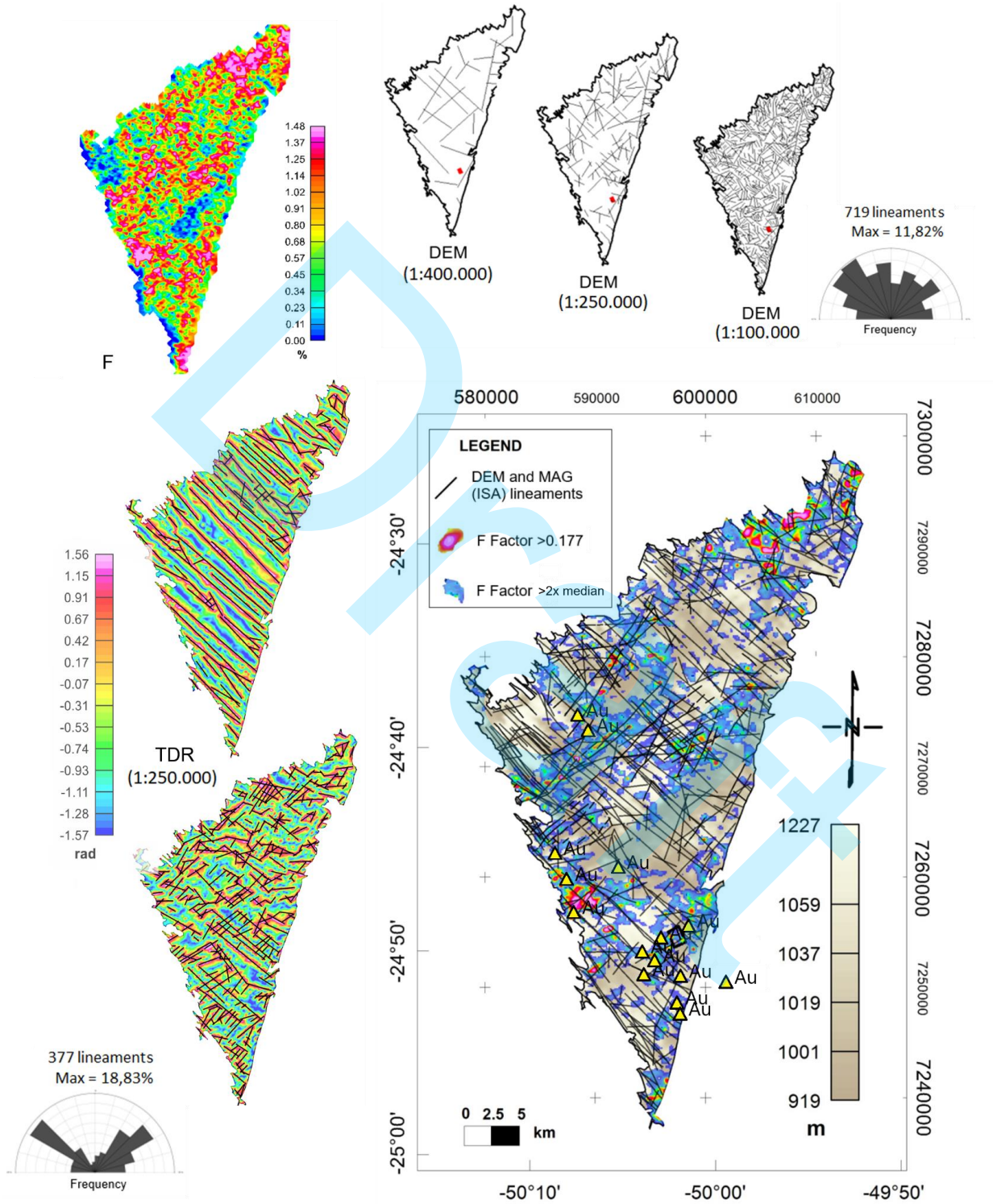

Figure 4 – Suggestive map for prospection of gold based on qualitative interpretation of integrated aerogeophysical datasets and DEM lineaments (CPRM, 2011). The Au symbol represents higher concentration of gold (≥ 25 ppb) in geochemical samples based on many authors (Lopes et al., 1969; Arioli and Moreton, 1982; Seoane, 1999; Mapa et al., 2016; Mapa et al., 2019).

The anomaly is probably related to a diabase dyke of the Ponta Grossa Arch. This interpretation is supported by the fact that basic rocks such as diabase are generally more weathered than acidic rocks such as rhyolite and quartz veins and are often enriched in magnetic minerals.

In the western part of the area, we observe a zone of high magnetic disturbance. Moderate magnetic values over rhyolites may indicate a magnetite-enriched zone, often associated with hydrothermal deposits formed under oxidizing conditions and with low sulfur content. As observed by Seoane (1999), magnetite often forms the matrix of hydraulic breccias of rhyolitic composition in the Castro Basin deposits.

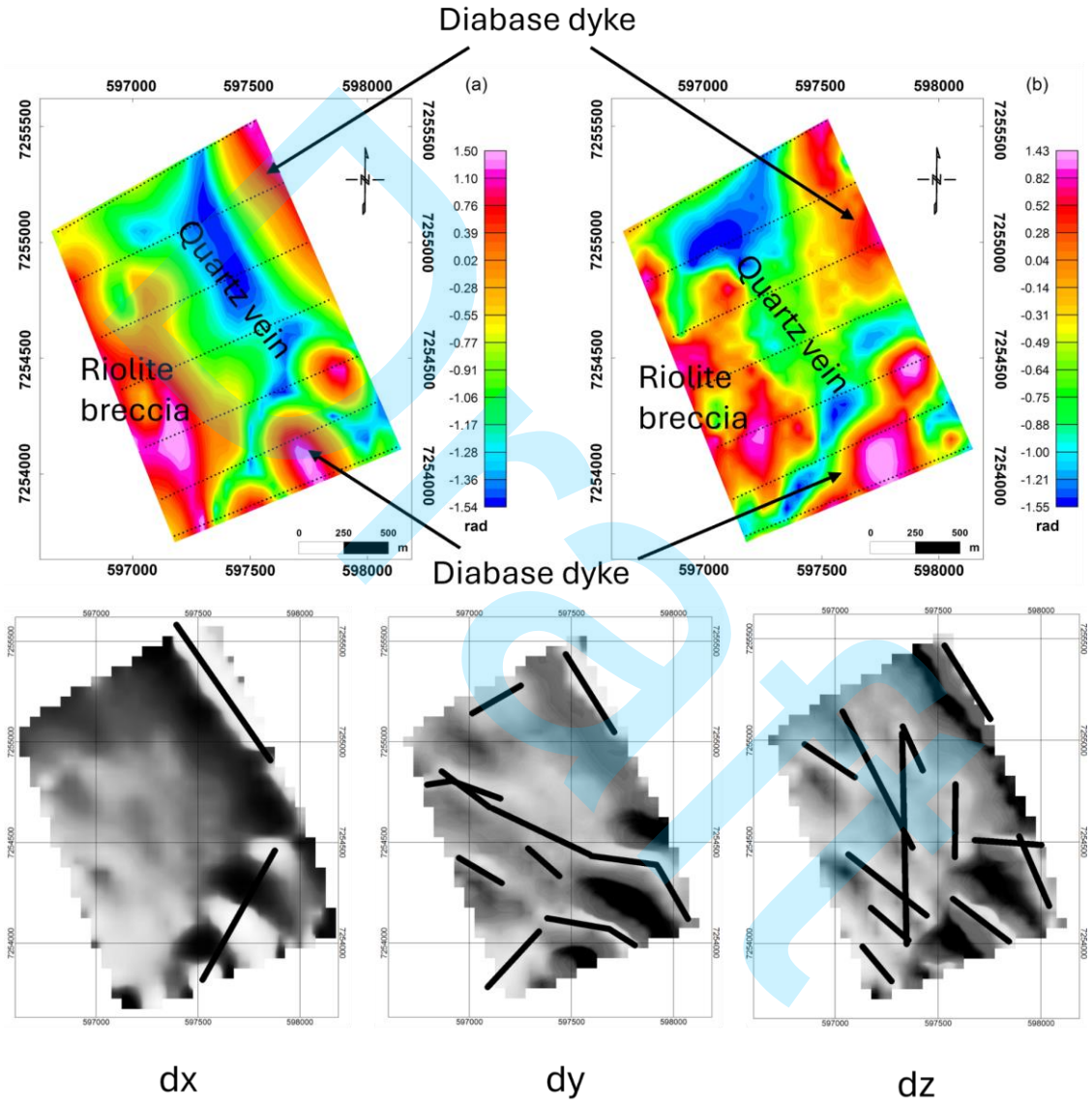

Figure 5 – Magnetic maps and interpretation on Torre Target made with ground data, where (a) is TDR_upw100m_RTP_TMI and (b) is TDR_DC145°_upw100m_RTP_TMI.

At profiles L1 and L2 (Figure 5), a strong, shallow IP anomaly is observed at the line extremities. This anomaly coincides with the high magnetic lineament identified in the magnetic and susceptibility maps of the Torre Polygon, suggesting a diachronic origin unrelated to the mineralization of interest.

The high chargeability observed at shallower depths (first 20 meters) in the initial part of L1 and other sections of L2, L3, and L4 is likely attributed to moist soil rich in clay minerals,

common in subtropical regions. These anomalies exhibit significant dimensions, extending laterally for hundreds of meters and vertically for more than 100 meters, often beyond the investigated depth in some areas.

The IP section of L2 reveals intermittent zones of high chargeability between stations 0-21 (0-560 meters), where the highest values potentially associated with gold mineralization are found at 50-250 meters. Two features within this line, at shallow and intermediate depths, are interpreted as quartz-adularia veins.

IP anomalies in epithermal systems are primarily caused by the membrane polarization effect due to the increased presence of illite-sericite group minerals. Chargeability values can reach several tens of mV/V. Additionally, disseminated metal sulfides within the matrix of hydrothermally altered rocks can enhance the chargeability effect through electrode polarization.

Deposits often occur near the main fault, characterized by conductive and well-defined vertical features in such environments. Searching for these signals can provide valuable clues for gold mineralization.

In L3, the highest and deepest anomalies are located between 160-370 meters, with the mineralized vein potentially extending from 320-520 meters near the surface. Similar patterns are observed in L4, where the anomaly appears at the beginning of the profile (0-200 meters) and again at 320-450 meters at shallow levels.

Atypical patterns are evident in L5 and L6. The topography becomes abruptly rougher at 350 meters, and the highest chargeability values are observed in the same locations. Quartz, being less susceptible to weathering processes, might be more preserved compared to background rocks like rhyolite, andesite, and siltstone, potentially indicating the presence of a tabular, horizontalized vein. In L6, this feature becomes more prominent and covers a larger area, with the chargeability anomalies clearly defining the structure. Along this line, the inflected vein extends over most sections (0-520 meters), with the main deposit likely located at 160-280 meters. At the end of L6, the anomaly corresponds to a pile of waste material extracted from a chalcedony quartz vein in a neighboring area (Figure 6).

At the end of profile L1, resistivity sections show a shallow to intermediate depth structure (Figure 7). This resistivity feature coincides with an IP anomaly, suggesting a possible association with a base dyke unrelated to gold mineralization.

Three main conductive discontinuities intersecting profiles L2, L3 and L4 are observed. A fourth low dip angle discontinuity intersects a resistive structure on L4 that projects to surface at approximately 280 meters. However, this structure has low to intermediate resistivity intervals.

On L5, the vein can be traced up to 600 meters. This interpretation is consistent with previous findings based on IP and topographic data. A similar feature appears on L6 (50-500 meters) but with a more intermittent pattern.

On profile L2 (725 meters), rhyolite outcrops have a resistivity of 2,000 Ohm.m. At the end of L6, a pile of waste material mined from the vein has a grade of 1 g/t Au. The geophysical characteristics of this stockpile were compared to the underlying rocks.

The predominance of two large conductive features on L5 reflects the high permeability of the environment. This line is adjacent to a lagoon located between L4 and L5 at 450-500 meters. The presence of lakes associated with rhyolitic domes and sediments controlled by ring fractures often results in the formation of filled channels (moats) (Seoane, 1999). The geophysical signature in the vicinity of this geomorphologic feature, in combination with other ore controls, strongly suggests the potential for mineralization.

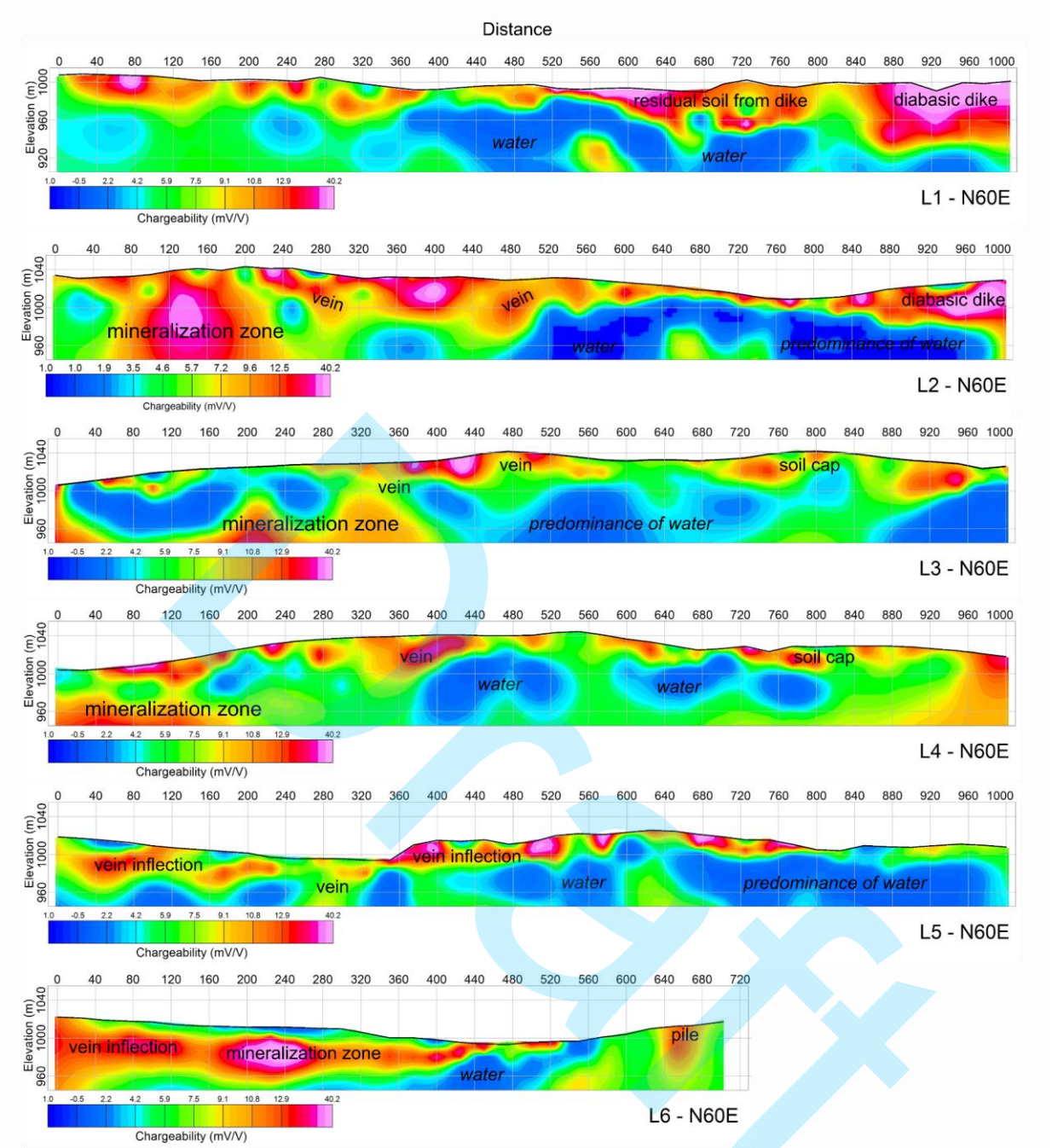

Figure 6 – Interpreted IP sections of L1-L6 showing the chargeability distribution of subsurface of Torre Target.

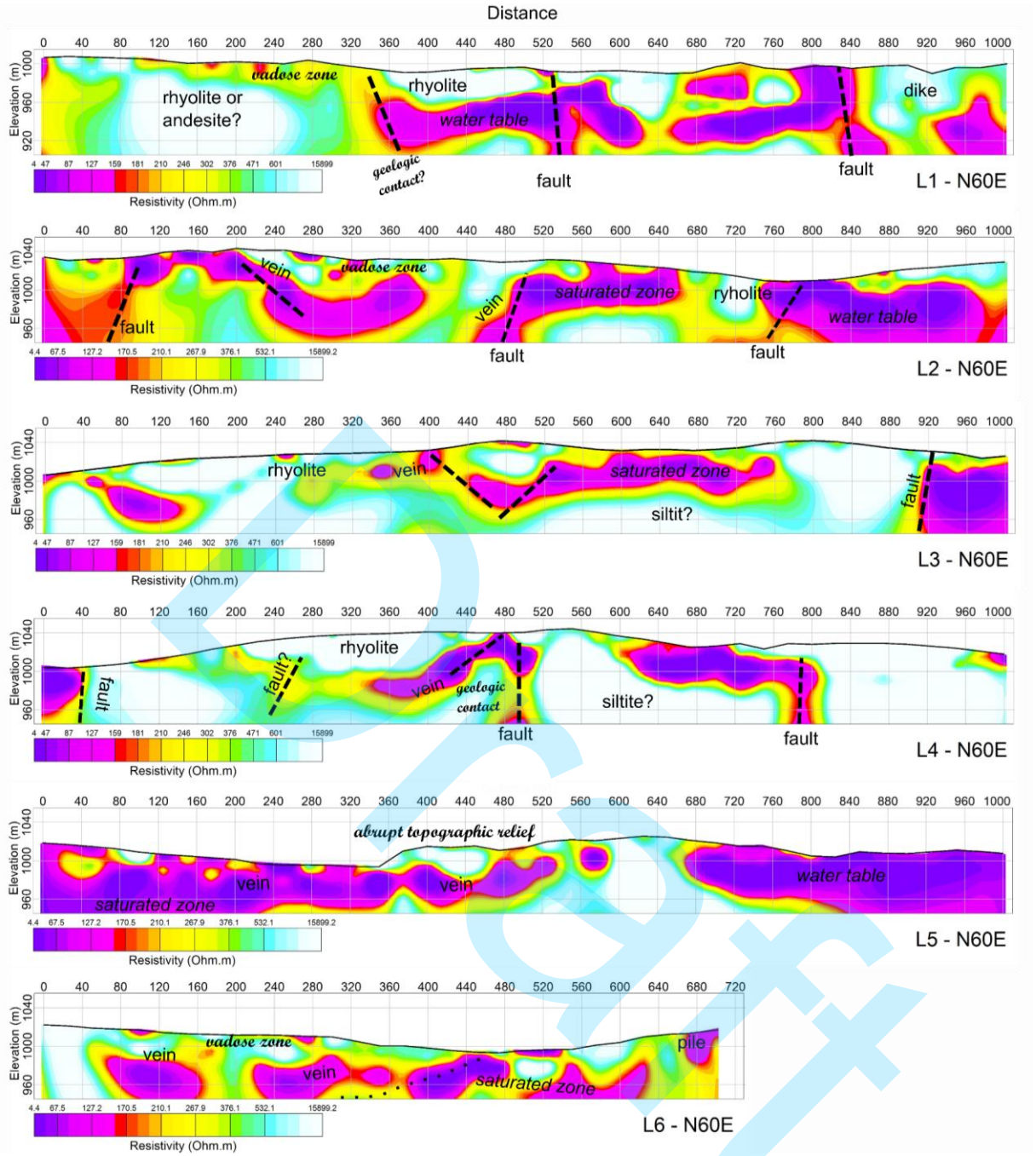

Figure 7 – Interpreted RES sections of L1-L6 showing the resistivity distribution of the subsurface of Torre Target.

Figure 8 shows a series of maps for each level of investigation, a total of eight slices combined to provide a 3D perspective of the anomalies. The mineralized NW trending quartz vein was identified on the first level and shows continuity through all levels to 100 meters where it widens significantly. The resistivity distribution maps clarified the structural behavior and revealed conductive lineaments that likely represent rock fractures. A prominent conductive lineament that mirrors the shape and direction of the surface vein appears at about 400-425 meters in Level 3, near the center of the survey line. In Level 4, a structure appears at nearly the same location as the mineralized vein and continues to the final level. In addition, a significant lithological discontinuity is observed in the opposite direction (NE) on all maps, northwest of the polygon. At the location where the quartz-chalcedony-adularia vein outcrops, a corresponding hill is visible on the digital elevation model.

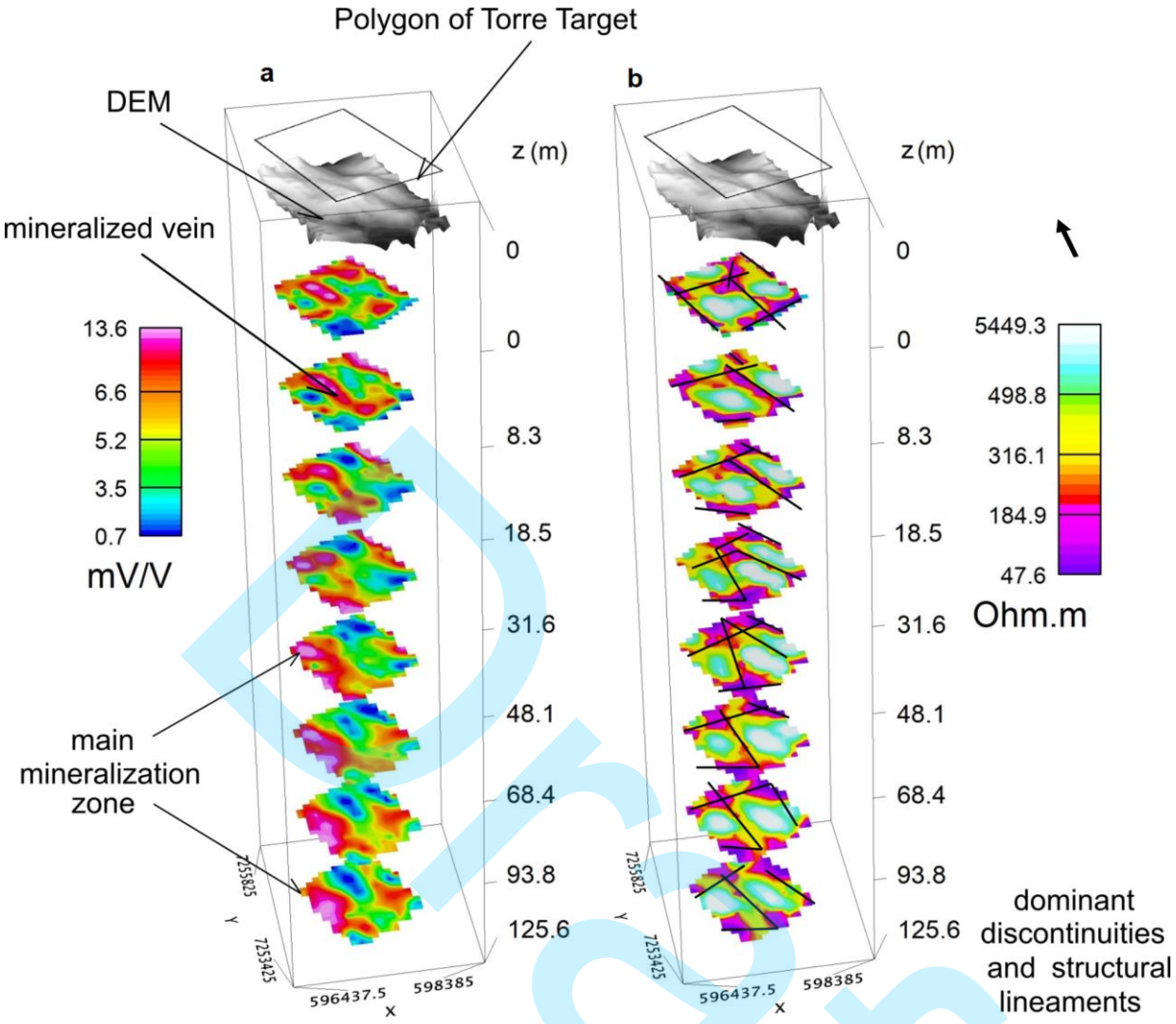

Figure 8 – Interpreted maps of levels of (a) IP and (b) Res of Torre Target in slices format.

To provide a more realistic representation, voxel models were constructed to depict the distribution of two geoelectric datasets in a three-dimensional space. One model simulated anisotropic conditions using chargeability and electrical resistivity data, while the other used isotropic conditions and chargeability data only. The Geokrige software was employed to create the first 3D model by interpolating cells using the kriging method with 140 (x), 170 (y), and 90 (z) blocks, assuming a trend of 250° and a dip of 60°.

The resistivity model was divided into 21 classes and merged with selected chargeability values ≥ 16.1 mV/V. A cutoff value of 8 was arbitrarily chosen to reduce the influence of the soil cap and exclude unrelated signals. A well-defined chargeability volume appeared in the southwest, suggesting a potential deposit. The quartz-chalcedony-adularia vein, a rock known for high Au concentrations, was also detected in the shallow levels of the model.

It is common to observe chargeability coinciding with conductive zones, often in vertical or well-defined structures. These features may indicate structural controls for ore deposits. A significant polarized volume was identified in the west, representing the main deposit within the surveyed area (Figure 9).

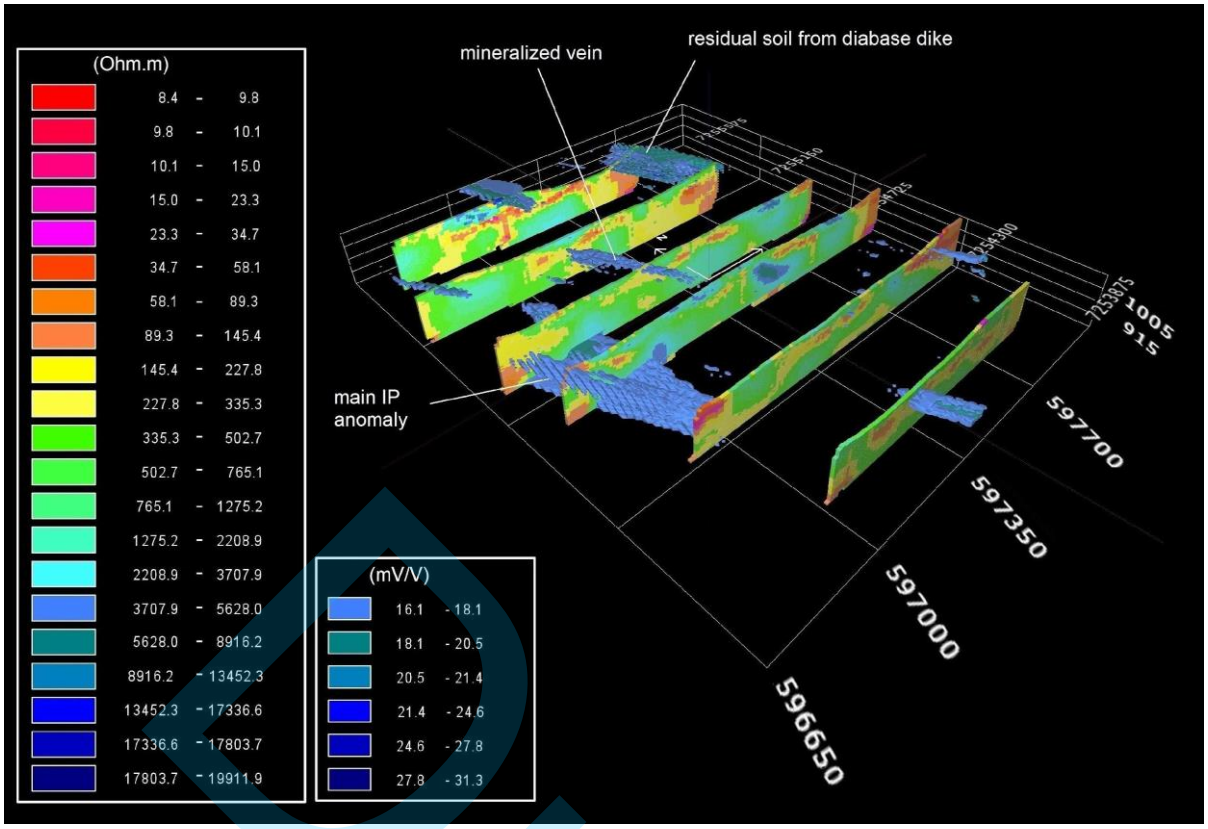

Figure 9 – Voxel model with resistivity sections and chargeability volume. High values of IP are seen in conductive regions and an important anomaly is revealed in the center west.

A second 3D model was created exclusively from the IP data and borehole information. This model utilized cubic cells of 50 m x 50 m x 35 m, employing the inverse distance weighting algorithm with logarithmic color distribution. The Geosoft/Seequent v.9 software was instrumental in generating this model.

To enhance interpretation, two iso-surface ranges were incorporated into the model: 8 mV/V, 10 mV/V, and 12 mV/V. These iso-surfaces were strategically positioned to intersect the drill holes, facilitating a direct comparison between the geologic section and the 3D IP model (Figure 10).

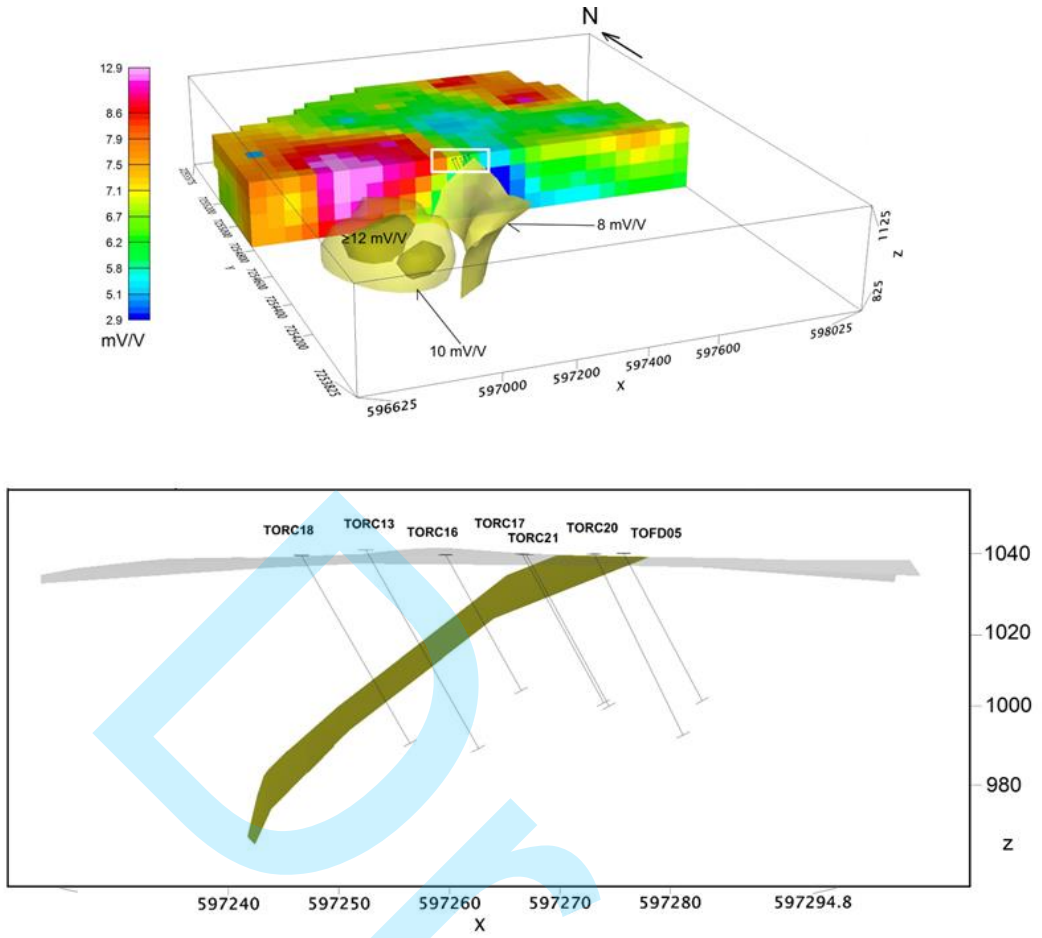

Figure 10 – IP voxel model with Vein Chargeability Anomalies. The model distinguishes three distinct chargeability thresholds: 8 mV/V, 10 mV/V, and greater than or equal to 12 mV/V.

A drill hole profile was planned to intersect the mineralized quartz vein at a location parallel to L3 and close to the outcrop. This site was selected to facilitate comparisons between geophysical data and geological mapping observations. Seven drill holes were completed, including one diamond drill (TOFD) and six reverse circulation drills (TORC). The precise location (X, Y), total depth, length, dip, and azimuth of each drill hole are listed in Table 2.

Table 2 – Drill hole location and survey measurements.

Hole (ID)	X	Y	Depth(m)	Length (m)	Dip (α)	Azimuth (θ)
TORC13	7254767	597229	47	88	-60°	60°
TORC16	7254770	597245	32	87	-60°	60°
TORC17	7254782	597259	36	64	-60°	60°
TORC18	7254761	597218	44	88	-60°	60°
TORC20	7254791	597263	44	72	-60°	50°
TORC21	7254774	597261	36	72	-60°	60°
TOFD05	7254786	597269	36	76	-60°	60°

Drill core samples were meticulously logged and analyzed at one-meter intervals. Each sample was carefully classified and sent to the laboratory for gold content evaluation. The resulting data was used to construct a detailed geologic section, accurately reconstructing and interpolating the geological features encountered in each borehole (Figure 11).

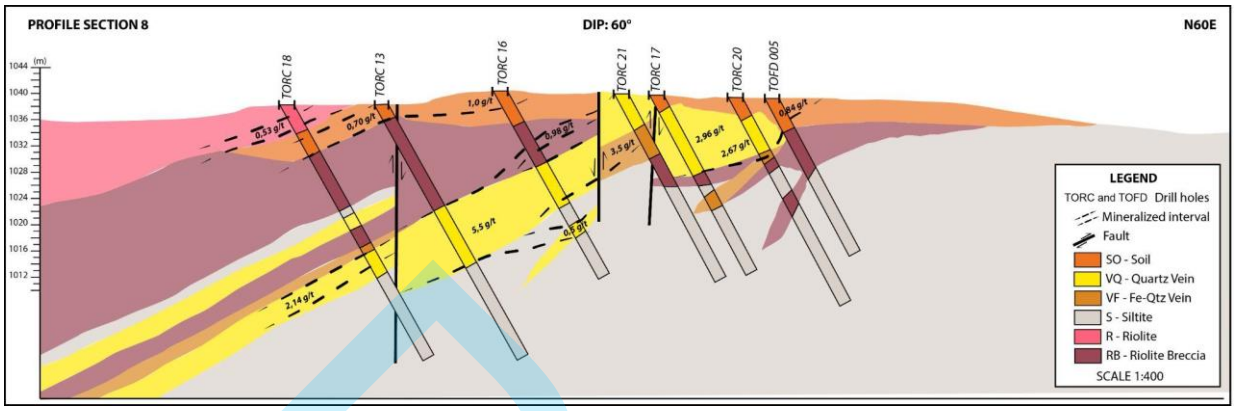

Figure 11 – Geologic profile based on borehole data analysis. The drill core samples validates the geophysical models in the map section.

DISCUSSION AND CONCLUSIONS

The IP anomalies identified in this study exhibit both superficial and deep-seated characteristics. The upper horizontal layer characterized by high chargeability, exceeding 10 meters in thickness in certain areas and prevalent across most sections, is primarily attributed to soil coverage rich in clay. This clay-rich layer likely resulted from the alteration of feldspathic rocks, a common erosion process influenced by the region's geological features and tropical climate.

Anomalies extending to greater depths are correlated with clay-rich materials, particularly those enriched in illite, and disseminated low-grade metal sulfides associated with quartz intrusions. These intrusions have hydrothermal origins and are known to be related to gold deposits.

Low-to-intermediate chargeability anomalies accompanied by very high resistivity values are interpreted as the geophysical signature of rhyolites. These rock formations are differentiated from saturated zones in the resistivity sections due to their inverse electrical response. Saturated zones exhibit higher conductivity and lower chargeability.

While the presence of andesite and siltstone rocks is acknowledged at subsurface depths, their electrical properties exhibit minimal variation, making them difficult to distinguish. To avoid misinterpretation and simplify the analysis, specific rock types were not assigned solely based on resistivity and IP values. The interpretation was conducted cautiously, relying on geological information derived from outcrops and drill core observations.

Beyond delineating the general location of solid rock, the resistivity data provided valuable insights into the detection and mapping of saturated zones and geological discontinuities. Verticalized conductive/low-resistivity features represent potential faults or lithological contacts, while horizontal features primarily indicate the water table or saturated zones (L1-L4). However, in some regions, these horizontal features may correspond to vein intrusions. This is particularly evident in sections L5 and L6, where a prominent sub-horizontal vein is clearly visible, coinciding with high IP anomalies in the same locations.

The integration of airborne geophysical methods, including gamma-ray spectrometry and magnetic data, has proven effective in identifying potential gold deposits within the Castro Basin. Mineralization in the region is often structurally controlled by large-scale lineaments within physically and chemically altered rocks.

The radiometric F factor map, highlighting radiometric signatures indicative of potassium enrichment, provides valuable insights into the hydrochemical processes associated with mineralization. In conjunction with the RTP and TDR maps, a comprehensive understanding of the structural network and geological units is achieved.

IP results were instrumental in delineating the main intrusion of quartz-adularia, chalcedony, and sericite-bearing rocks. Furthermore, these results identified a promising mineralization zone characterized by elevated clay content and disseminated metal sulfides within veins and felsic rocks. The quartz vein exhibited high resistivity and conductive vertical anomalies indicative of normal faults and contacts.

Magnetometry played a crucial role in revealing intermediate-amplitude magnetic signatures associated with the concentration of magnetite within hydraulic breccias and rhyolites. These rock types are linked to the same hydrothermal alteration events. The northwest-oriented magnetic gradient and low topographic alignment suggest the presence of diabase dikes, which are more susceptible to weathering compared to quartz-adularia veins. This distinction helps to clarify the IP data by separating the signature of the alteration zone from unrelated dykes.

The 3D models generated in this study enable the estimation of the area and volume of a confirmed deposit within the Torre Target. However, further validation through drilling programs is essential to substantiate these findings.

ACKNOWLEDGEMENTS

The authors gratefully acknowledge the financial support provided by the CAPES Foundation, Ministry of Education of Brazil (grant no. 88882.381511/2011-01), and the National Council for Scientific and Technological Development (CNPq, Brazil) (grant no. 303826/2018-5). Fellowships awarded to F. Antonelli and F.J.F. Ferreira were funded through these grants.

The authors would like to express their sincere gratitude to the Companhia de Pesquisa de Recursos Minerais (CPRM, Geological Survey of Brazil) and Verdau Mineração Ltda for granting permission to use the geological and geophysical data, which were essential to the development of this research.

REFERENCES

Airo, M.L., 2001, Aeromagnetic and aero radiometric response to hydrothermal alteration. Geological Survey of Finland, 32, 273-302, https://doi.org/10.1023/A:1015556614694.

Airo, M.L., Mertanen, S., 2008, Magnetic signatures related to orogenic gold mineralization, Central Lapland Greenstone Belt, Finland. J. of Applied Geophysics, 64, 14-24, https://doi.org/10.1016/j.jappgeo.2007.10.003.

Allis, R.G., 1990, Geophysical anomalies over epithermal systems. J. of Geochemical Expl., 36, 339-374, https://doi.org/10.1016/0375-6742(90)90060-N.

Almeida, R. P., Janikian, L., Fragoso-Cesar, A. R. S., & Fambrini, G. L. 2010. The Ediacaran to Cambrian Rift System of Southeastern South America: Tectonic implications. The Journal of Geology, 118, 2, 145–161. https://doi.org/10.1086/649817.

Arioli, E.E., Moreton, L.C., 1982, Projeto Castro - Relatório de Etapa. Relat. lnt. Curitiba, Brazil: Mineropar - Minerais do Paraná S. A., 106 pp.

Baranov, V., Naudy, H., 1964, Numerical Calculation of the Formula of Reduction to the Magnetic Pole, Geophysics, 29, 1, 67-79, https://doi.org/10.1190/1.1439334.

Briggs, I.C., 1974, Machine contouring using minimum curvature. Geophysics, 39, 39-48, https://doi.org/10.1190/1.1440410.

CPRM – Brazilian Geological Survey, 2011, Lasa Prospecções S.A. Projeto Aerogeofísico Paraná - Santa Catarina, Texto Técnico, 326 pp.

Mapa, F. B., Marques, I. P., Turra, B. B., Caltabeloti, F. P., Palmeira, L. C. M., Severino, R. R., Campos, F. F., Silva, A. D. R. da, & Tavares, F. M., 2016, Occurrence of free gold in hydrothermally-altered volcanic rocks at Castro Basin, state of Paraná, Brazil: Perspectives for new potential areas. CPRM – Geological Survey of Brazil.

Mapa, F. B., Marques, I. P., Turra, B. B., and Palmeira, L. C. M., 2019, Áreas de relevante interesse mineral (ARIM): geologia e recursos minerais da Bacia de Castro, estado do Paraná. CPRM.

Dentith, M., and Mudge, S.T., 2014, Geophysics for the Mineral Exploration Geoscientist. Cambridge University Press, 454 pp.

Feebray, C.A., Hishida, H., Yoshika, K., Nakayama, K., 1998, Geophysical expression of low sulphidation epithermal Au-Ag deposits and exploration implications - examples from the Hokusatsu region of SW Kyushu, Japan. Resource Geology, 48, 75−86, https://doi.org/10.1111/j.1751-3928.1998.tb00008.x

Hedenquist, J.W., Arribas Jr., A., Gonzalez-Urien, E., 2000, Exploration for epithermal gold deposits. Reviews in Economic Geology, 13, 245-277, https://doi.org/10.5382/Rev.13.07

Hoover, D.B., Heran, W.D., Hill, P.L., 1992, The geophysical expression of selected mineral deposit models. U.S. Department of the Interior Geological Survey, Open-file report, 92-557.

Irvine, R.J., and Smith, M.J., 1989, Geophysical exploration for epithermal gold deposits. Geochemical Exploration, 36, 375-412, https://doi.org/10.1016/0375-6742(90)90061-E.

Li, X., 2008, Magnetic reduction-to-the-pole at low latitudes: observations and considerations. Leading Edge, 27, 8, 990–1002, http://dx.doi.org/10.1190/1.2967550.

Lopes, J.A., Trein, E., Muratori, A., Palka, J., Fuck, R.A., 1966, Folha Geológica de Castro. Com. Carta Geológica do Paraná, Mapa Geológico em escala 1:50.000.

Miller, H.G., Singh, V., 1994, Potential field tilt – A new concept for location of potential field sources. J. Applied Geophysics, 32, 213-217, https://doi.org/10.1016/0926-9851(94)90022-1.

Morrell, A.E., Locke, C.E., Cassidy, J., Mauk, J.L., 2011, Geophysical Characteristics of Adularia-Sericite Epithermal Gold-Silver Deposits in the Waihi-Waitekauri Region, New Zealand. J. Economic Geology, 106, 1031-1041, https://doi.org/10.2113/econgeo.106.6.1031.

Raposo, M.I.B., Ernesto, M., 1995, An early cretaceous paleomagnetic pole from Ponta Grossa dikes (Brazil): implications for the south American Mesozoic apparent polar wander path. J. Geophysics, Research Solid Earth, 100, 20095–20109, https://doi.org/10.1029/95JB01681.

Reis Neto, J.M., Moro, R. de P.X., Siga, Jr. O., 1994, Grupo Castro: Idade e Implicações Tectônicas. Congr. Bras. Geologia., 38, Camboriú. Bol. de Res. Exp. 2, Brazil, 394-395.

Reynolds, J. M., 2011, An Introduction to Applied and Environmental Geophysics. Preview, 2011, 33-40.

Ribeiro, V. B., Mantovani, M., Louro, V. H. A. 2015. Aerogamaespectrometria e suas aplicações no mapeamento geológico. Terra e Didática, Campinas, SP, v. 10, n. 1, p. 29–51. DOI:

https://doi.org/10.20396/td.v10i1.8637386.

Scott, B.L, Dickson, K.M., 1997, Interpretation of aerial gamma-ray surveys adding the geochemical factors. Journal of Australian Geology & Geophysics, 17, 2, 187-200.

Seoane, J.C.S., 1999, Geologia do ouro epitermal de Castro. Ph.D. thesis, Universidade Federal de Campinas – Unicamp, São Paulo, Brazil, 216 pp.

Serrano, V.D., 2018, Modelagem geológica e avaliação dos recursos minerais de ouro e prata na Fazenda São Daniel - Carambeí-PR. M.Sc. dissertation, Universidade de São Paulo - USP, São Paulo, Brazil, 90 pp.

Silva, D.C., and Vaine, M.E.E., 2001, Atlas comentado da geologia e dos recursos do Estado do Paraná. Mineropar, Curitiba, Paraná, Brazil. 125 pp.

Weihermann, J.D., Ferreira, F.J.F., Oliveira, S.P., Cury, L.F., Souza J., 2018, Magnetic interpretation of the Paranaguá Terrane, southern Brazil by signum transform. Journal of Applied Geophysics, 154, 116-127, https://doi.org/10.1016/j.jappgeo.2018.05.001.

White, N.C., Hedenquist, J.W., 1995, Epithermal Gold Deposits: style, characteristics and exploration. SEG Newsletter, 23, 1, 9-23. https://doi.org/10.5382/SEGnews.1995-23.fea.

Antonelli, F.: conceptualization, data acquisition, data processing, models development and writing; **Stevanato, R.:** data acquisition, data processing and models development; **Rodizes, A.**: conceptualization, writing, discussion of results; **Serrano, V. D.**: data acquisition, geological data; **Yamamoto, J. K.**: data modelling; **Abreu, G.**: reviewing, discussion of results; **Ferreira, F. J. F.**: discussion of results, reviewing, supervision; **Fries, M.:** discussion of results, supervision.